RSC Advances

PAPER

View Article Online
View Journal | View Issue

Cite this: *RSC Adv.*, 2026, **16**, 22698

Designing green-emissive Cu,N-codoped carbon dots by pyrolysis of aromatic precursors and application in sensing of Fe(III) and Cr(VI)

Thien-Phuc Nguyen, [a] Nhu Vo Thi Thu, [a] Minh Hao Hoang, [a] Nham Linh Nguyen, [a] Thanh-Sang Nguyen, [a] Dat Nguyen, [a] Nhiem Ly, [a] Thanh Tuyen Nguyen,[a] Phuong V. Pham [b] and Dinh Khoi Dang *[a]

Detecting toxic transition metal ions using carbon dots (CDs) as fluorescent probes is efficient and sensitive, yet the rational design of CDs with controlled composition and tunable sensing selectivity remains a key challenge. Herein, we report the one-step, solvent-free pyrolysis synthesis of novel fluorescent Cu,N-co-doped carbon dots (Cu,N-CDs) from two aromatic precursors, *p*-aminosalicylic acid (PAS) and copper(II) acetylacetonate ($Cu(acac)_2$), under mild conditions (170 °C, 3 h). The resultant Cu,N-CDs exhibited strong green fluorescence with a maximum emission at 495 nm under excitation at 395 nm and a quantum yield of 14.9%. Without further surface modification, these Cu,N-CDs demonstrated high performance as dual fluorescent probes for the simultaneous detection of Fe(III) and Cr(VI) ions. Upon excitation at 395 nm, introduction of either Fe(III) or Cr(VI) at 100 μM resulted in pronounced fluorescence quenching by factors of 50.3 and 3.53, respectively, through two mechanistically distinct pathways: Fe(III) quenching proceeds *via* formation of a non-fluorescent coordination complex with surface functional groups of the Cu,N-CDs, while Cr(VI) quenching arises primarily from the inner filter effect. The Cu,N-CDs offered high selectivity with low limits of detection for Fe(III) (1.48 μM) and Cr(VI) (19.6 nM). The scalable, solvent-free synthetic strategy and the dual-analyte sensing capability demonstrated here position these Cu,N-CDs as promising platforms for practical deployment in environmental water monitoring, food safety screening for detection of heavy metal pollutants.

Received 23rd January 2026
Accepted 25th April 2026

DOI: 10.1039/d6ra00625f

rsc.li/rsc-advances

1. Introduction

Low cost, highly sensitive sensors for the determination of toxic heavy metals are in high demand. Due to being non-biodegradable, heavy metals accumulate in the environment and in the food chain, deteriorating the health of animals and humans.[1] Iron is one of the most abundant elements in the Earth's crust and is ubiquitous in natural water systems, where Fe(III) commonly reaches concentrations of 7–15 mg L^{-1} in natural groundwater.[2] While iron is an essential micronutrient, excess Fe(III) poses significant health risks through its participation in Fenton-type and Haber–Weiss reactions, generating reactive oxygen species (ROS) including hydroxyl radicals.[3] Cellular iron overload has been reported to induce oxidative stress, defined as an increase in the steady-state concentration of oxygen radical intermediates, causing oxidative damage to lipid membranes and contributing to hepatotoxicity, cardiovascular disease, and neurodegenerative disorders.[4] Hexavalent chromium, Cr(VI), presents an even more acute environmental and public health threat. Existing in highly soluble and mobile anionic forms (CrO_4^{2-} and $Cr_2O_7^{2-}$), Cr(VI) exhibits approximately 100-fold higher toxicity than its trivalent counterpart Cr(III),[5] and the World Health Organization (WHO) restricts its concentration in drinking water to 0.05 mg L^{-1}.[6] Cr(VI) is classified as a Group 1 human carcinogen by the US EPA and IARC, with epidemiological studies demonstrating elevated risks of lung, prostate, bladder, and hematological cancers in exposed populations.[7] At the molecular level, Cr(VI) exerts its toxicity through multiple mechanisms including genomic instability, oxidative DNA adduct formation, and epigenetic silencing of tumour suppressor genes.[8] Chronic exposure additionally causes systemic damage including allergic reactions, anemia, gastrointestinal injury, and reproductive toxicity.[9]

Given the sub-milligram-per-litre regulatory thresholds for both Fe(III) and Cr(VI) in drinking water, the development of sensitive and selective analytical methods for their detection is of paramount importance. Conventional laboratory techniques—including atomic absorption spectroscopy (AAS), inductively coupled plasma mass spectrometry (ICP-MS), and high-performance liquid chromatography (HPLC)—while capable of achieving trace-level detection, suffer from several

[a]*Faculty of Chemical and Food Technology, Ho Chi Minh City University of Technology and Engineering, 01 Vo Van Ngan Street, Thu Duc Ward, Ho Chi Minh City, 700000, Vietnam. E-mail: khoidd@hcmute.edu.vn*

[b]*Department of Physics, National Sun Yat-sen University, Kaohsiung 80424, Taiwan*

practical limitations that restrict their deployment for routine environmental monitoring. These methods necessitate bulky, expensive instrumentation, require highly trained personnel, involve time-consuming sample preparation, and are fundamentally unsuitable for on-site or real-time analysis.[10] Colorimetric sensors, while simpler, often provide only qualitative or semi-quantitative results with limited sensitivity.[11] Electrochemical sensors have emerged as a promising alternative due to their portability and low cost; however, they are prone to sensor drift, biofouling, and interference in complex water matrices, limiting their long-term reliability.[12] These limitations highlight a pressing need for sensitive, selective, portable, and cost-effective detection platforms capable of simultaneous Fe(III) and Cr(VI) determination in real environmental samples.

Fluorescent methods have become popular for detecting metal ions in both biological and environmental samples due to their operational simplicity and minimal sample preparation.[13] As fluorescent materials, CDs possess valuable characteristics such as high photostability,[14] hydrophilicity or hydrophobicity,[15] capability of functionalization,[16] and biocompatibility.[17] The fluorescence of CDs can be quenched by metal ions, a property that has been utilized for the selective and sensitive detection of transition metal ions.[18] Typical bottom-up CDs syntheses are hydrothermal and solvothermal routes, but both methods carry inherent limitations. Hydrothermal synthesis, while relatively eco-friendly due to the use of water as solvent, is constrained by the limited volume of autoclave reactors, making it unsuitable for large-scale industrial production; additionally, the prepared CDs often contain impurities that are difficult to separate and purify, and particle size is challenging to control.[19] Solvothermal synthesis, which employs organic solvents such as benzene, DMF, or DMSO under high temperature and pressure, introduces additional hazards including safety risks from pressurized systems, high energy consumption, and environmental concerns associated with the use of expensive, toxic, and non-renewable solvents that require special post-reaction treatment.[20] Furthermore, many solvothermal methods require the addition of toxic external reagents as doping agent of other elements (N, P, S, and metals) into CDs, increasing synthetic complexity.[21] In contrast, the solvent-free pyrolytic strategy adopted in the present work offers several distinct advantages. By eliminating the need for any solvent, the approach avoids the safety hazards associated with high-pressure sealed autoclaves, removes the cost and environmental burden of organic solvents, and simplifies post-synthesis workup. The method is also amenable to easy operation, scalable production, and fast reaction times.[22] These combined attributes position the solvent-free pyrolytic strategy as a meaningful advance over existing hydrothermal and solvothermal methods for the green synthesis of fluorescent CDs for Fe(III) and Cr(VI) sensing.

In this study, the choice of PAS as the primary carbon precursor is deliberate and multifaceted. PAS is structurally distinctive in that it combines all of these desirable features within a single molecule: an aromatic benzene ring, an amino group ($-NH_2$), a carboxyl group (–COOH), and a hydroxyl group (–OH). The presence of the $-NH_2$ group is essential for nitrogen doping. Moreover, surface $-NH_2$, –COOH, and –OH groups collectively provide rich coordination sites for interaction with metal ions, which is fundamental to the fluorescence quenching sensing mechanism. Furthermore, PAS has been reported as a productive precursor for CD synthesis using hydrothermal and solvothermal routes, generating N-doped CDs with tunable multicolor emission, a quantum yield of ~16%, and selective Fe^{3+} sensing capability in living cells.[23] Additionally, the inclusion of $Cu(acac)_2$ as a co-precursor is motivated by the documented role of copper doping in a manner directly beneficial to sensing selectivity. The incorporation of Cu into CDs has been demonstrated to generate materials with strong selectivity for Cr(VI) detection *via* fluorescence quenching.[24] The use of an acetylacetonate ligand in $Cu(acac)_2$ is also significant: acetylacetonate complexes are widely used in organic and materials synthesis and it has been used to synthesize Cu-doped CDs.[25,26] Taken together, PAS provides the N-rich aromatic carbon framework needed for high fluorescence quantum yield and Fe^{3+} coordination, while $Cu(acac)_2$ introduces Cu doping that confers selective sensitivity toward Cr(VI), enabling the dual-analyte sensing capability of the present system. To the best of our knowledge, the synthesis of Cu,N-CDs by pyrolysis of PAS and $Cu(acac)_2$ has not been studied before.

2. Experimental

2.1. Chemicals

p-Aminosalicylic acid (PAS), copper(II) acetylacetonate ($Cu(acac)_2$), and quinine sulfate dihydrate (QS) were supplied by Sigma-Aldrich (United States). Additional chemicals, including potassium chloride (KCl), sodium chloride (NaCl), calcium chloride ($CaCl_2$), cadmium sulfate ($CdSO_4$), cobaltous sulfate ($CoSO_4$), copper sulfate ($CuSO_4$), magnesium sulfate ($MgSO_4$), manganese sulfate ($MnSO_4$), zinc sulfate ($ZnSO_4$), potassium dichromate ($K_2Cr_2O_7$) and ferric chloride ($FeCl_3$), were acquired from Xilong Co. Ltd (China). All experimental solutions were prepared using deionized water.

2.2. Apparatus

Transmission electron microscopy (TEM) and high-resolution transmission electron microscopy (HRTEM) analyses were conducted using the JEI Tecnai G2F30 S-Twin instrument (Japan) at an accelerating voltage of 200 kV. The surface charge and size distribution of Cu,N-CDS were determined with a Zetasizer Pro (Malvern Instruments Ltd). X-ray photoelectron spectroscopy (XPS) data were collected utilizing a Leybold system (Germany) and processed on an ESCALAB250 Theta Probe XPS platform. Fourier transform infrared (FT-IR) spectra of powdered Cu,N-CDs samples were acquired using a Jasco FT-IR 4700 spectrometer (Japan), spanning a range of 4000–400 cm^{-1}. UV-visible spectral measurements were performed on a HITACHI UH5300 UV-visible spectrophotometer (Japan) employing a 1 × 1 cm optical path quartz cell. Photoluminescence (PL) spectra were obtained *via* a Horiba Fluoro-Max Plus fluorescence spectrophotometer (Japan). X-ray diffraction (XRD) patterns were recorded on a Bruker D8

Advance diffractometer (Bruker, USA) to examine the phase composition and crystallinity of the Cu,N-CDs. The elemental composition was determined by energy-dispersive X-ray (EDX) spectroscopy using a spectrometer integrated into a Hitachi TM4000 scanning electron microscope (Hitachi, Japan).

2.3. Synthesis of Cu,N-codoped carbon dots (Cu,N-CDs)

The novel Cu,N-CDs were synthesized *via* a straightforward, solvent-free procedure. Initially, 400 mg of PAS and 100 mg of $Cu(acac)_2$ were finely ground and thoroughly blended in a ceramic mortar to achieve a uniform powder. This mixture was transferred into a ceramic crucible, which was then sealed with aluminum foil. Subsequently, the covered crucible was heated at 170 °C for three hours using a heating mantle. Upon completion, the crucible was cooled to ambient temperature and removed from the mantle. Thereafter, 10 mL of deionized water was added, and the contents were subjected to ultrasonic dispersion for five minutes. The resulting suspension was first filtered through filter paper, followed by filtration with a 0.22 μm membrane to remove larger particulates. The resultant bright yellow solution was purified against deionized water using dialysis tubing (1 kDa pore size) to eliminate impurities and unreacted materials. Control samples utilizing either PAS or $Cu(acac)_2$ alone as precursors were prepared following an identical protocol. The synthetic procedure is designed based on two purposes. First, the pyrolysis temperature is 170 °C because of: (i) melting of PAS (melting point: ~150 °C); (ii) sublimation of $Cu(acac)_2$ (having relatively low vapor pressure of 8.83 kPa at 140 °C).[27] Second, before filtration through filter paper, 10 mL of deionized water was added and the mixture was subjected to ultrasonic dispersion for 5 minutes to ensure complete and homogeneous dispersion of the carbon product prior to filtration, preventing aggregation losses.

2.4. Determination of the quantum yield

The quantum yield (QY) of the synthesized Cu,N-CDs was determined using a widely recognized relative method. Quinine sulfate (QY = 54% in 0.1 M H_2SO_4) served as the reference standard. To minimize re-absorption effects, both the Cu,N-CDs sample solution and the reference were diluted to ensure that the absorption intensity remained below 0.2. Absorption and emission measurements were then conducted in a 1 × 1 cm quartz cuvette containing the respective solutions. Measurements were performed using a FluoroMax Plus fluorescence spectrophotometer (Horiba). The quantum yield (QY) of the synthesized Cu,N-CDs was subsequently calculated according to the following equation:

$$Q = Q' \times \frac{A'}{I'} \times \frac{I}{A} \times \frac{n^2}{n'^2}$$

Q, I, A, and n respectively denote the quantum yield, integrated emission intensity, optical density, and refractive index (1.33 for water) of the sample under investigation. The prime symbol ($'$) designates the reference dye with a known quantum yield.

2.5. Effect of environmental factors: storage time, ionic strength, and pH

The effect of pH on Cu,N-CDs fluorescence was evaluated using buffer solutions spanning pH 1–13. The composition of each buffer is provided in Table S1 (SI). Solution of Cu,N-CDs is diluted to a concentration of 4.8 μg mL^{-1} before measurement. Storage stability was assessed by monitoring the fluorescence intensity of the Cu,N-CDs over 10 weeks at room temperature in dark condition until use. Ionic strength stability was evaluated by measuring fluorescence intensity in the presence of NaCl solutions at varying concentrations (up to 2 M).

2.6. Detection of heavy metal ions

The fluorescent detection probe was prepared by diluting the Cu,N-CDs with deionized water to obtain a solution at a concentration of 4.8 μg mL^{-1}. The fluorescence emission intensity at 495 nm for the blank sample (excitation at 395 nm) was recorded as F_0. For quantifying the relationship between concentrations of metal ions (Fe(III) or Cr(VI)) and fluorescence intensity, 100 μL aliquots of metal ion solutions at varying concentrations (10 μM to 10 mM) were added to 10 mL of the aforementioned Cu,N-CDs solution. After allowing several minutes for equilibration, the fluorescence intensity (F) of each sample was measured. Selectivity towards Fe(III) or Cr(VI) was evaluated by introducing other related analogues, including K(I), Na(I), Ca(II), Cd(II), Co(II), Cu(II), Mg(II), Mn(II), and Zn(II) following the same procedure.

2.7. Statistical analysis

All sensing experiments were performed in triplicate ($n = 3$). Reported fluorescence intensity values represent the mean of three independent measurements, and error bars in figures represent the standard deviation (SD). The limits of detection (LOD) and quantification (LOQ) were calculated as LOD = $3.3(\sigma/S)$ and LOQ = $10(\sigma/S)$, where σ is the standard error of the calibration curve and S is the slope of the calibration curve.[28]

3. Results and discussion

3.1. Preparation of Cu,N-CDs

Photoluminescence (PL) in CDs has traditionally been attributed to either quantum confinement effects or surface-related states, including oxygen-containing functional groups and carbon-sp^2 domains. Generally, PL emission are widely considered to arise from the interplay between the intrinsic aromatic framework (sp^2 hybridization) and extrinsic contributions from functional groups and disordered regions such as defects and sp^3 carbon.[29] The formation pathway of CDs is strongly dictated by the chemical nature of the precursors. Conventional synthetic strategies typically employ either aromatic compounds or citric acid derivatives.[30] Hydrothermal and solvothermal methods are widely adopted for aromatic precursors, whereas pyrolysis is most often applied to citric acid systems. The pyrolytic transformation of aromatic precursors remains largely unexplored.

To address this gap, we selected PAS as a representative aromatic precursor, chosen for its conjugated framework and functional substituents, to probe the feasibility of pyrolytic conversion. As depicted in Scheme 1, PAS and $Cu(acac)_2$ were combined in a solvent-free, solid-state reaction and subjected to thermal treatment at 170 °C for three hours. This streamlined process yielded Cu,N-CDs following purification. The resulting aqueous solution was readily tunable, with concentrations diluted down to 4.8 μg mL^{-1} for subsequent spectroscopic measurements and application studies.

Analysis of the digital images in Fig. 1 demonstrates that employing a single precursor, either $Cu(acac)_2$ or PAS, produces negligible or no detectable color emission. Strikingly, the combination of both precursors yields a solution with intense green emission at 495 nm under UV excitation at 395 nm. Previous reports have utilized PAS in conjunction with various reagents under hydrothermal or solvothermal conditions to synthesize carbon dots, including tartaric acid[31] and polyethyleneimine.[32] Our work establishes, for the first time, a facile, solvent-free pyrolytic route to Cu,N-CDs using PAS as the primary precursor in combination with $Cu(acac)_2$.

We systematically screened a series of carbon sources under identical pyrolysis conditions; the results are shown in Fig. 1b and summarized in Table 1. The screening reveals that the presence of a primary amine ($-NH_2$) group is the critical structural requirement for producing fluorescent CDs under these conditions. The $-NH_2$ group can form C=N bonds through Schiff base condensation during pyrolysis, either incorporating nitrogen into the aromatic system or extending the conjugated chain, resulting in a red shift.[33]

This outcome can be rationalized as follows. PAS offers distinct structural advantages as a self-contained CD precursor: 1/the pre-formed benzene ring serves as a nucleus for sp^2 graphitic domain formation during pyrolysis, bypassing the energy-intensive aromatisation step that limits aliphatic precursors such as citric acid; 2/the $-NH_2$ group at the para position enables direct nitrogen incorporation into the carbon framework, which is confirmed by FTIR and XPS characterisation (Sections 3.2.3 and 3.2.4); and 3/the –OH and –COOH groups drive condensation and partial decarboxylation during pyrolysis while preserving surface functional groups that confer water solubility and metal ion coordination capability. It should be noted, however, that this interpretation applies specifically to pyrolysis in the presence of $Cu(acac)_2$, and the possible role of the Cu precursor in this condensation process is discussed in Section 3.2.5.

3.2. Instrumental analysis of CDs

3.2.1. TEM analysis. The structural and morphological characteristics of the synthesized Cu,N-CDs were investigated using transmission electron microscopy (TEM) and high-resolution TEM (HRTEM). For TEM sample preparation, a diluted aqueous solution of Cu,N-CDs was drop-cast onto carbon-coated copper grids. Fig. 2a presents an HRTEM image of the Cu,N-CDs, revealing a lateral size distribution between 3.8 and 13.2 nm, with an average diameter of 9.13 ± 2.61 nm. The corresponding particle size histogram in Fig. 2b confirms this distribution. These dimensions are consistent with previous reports of CDs synthesized *via* hydrothermal routes

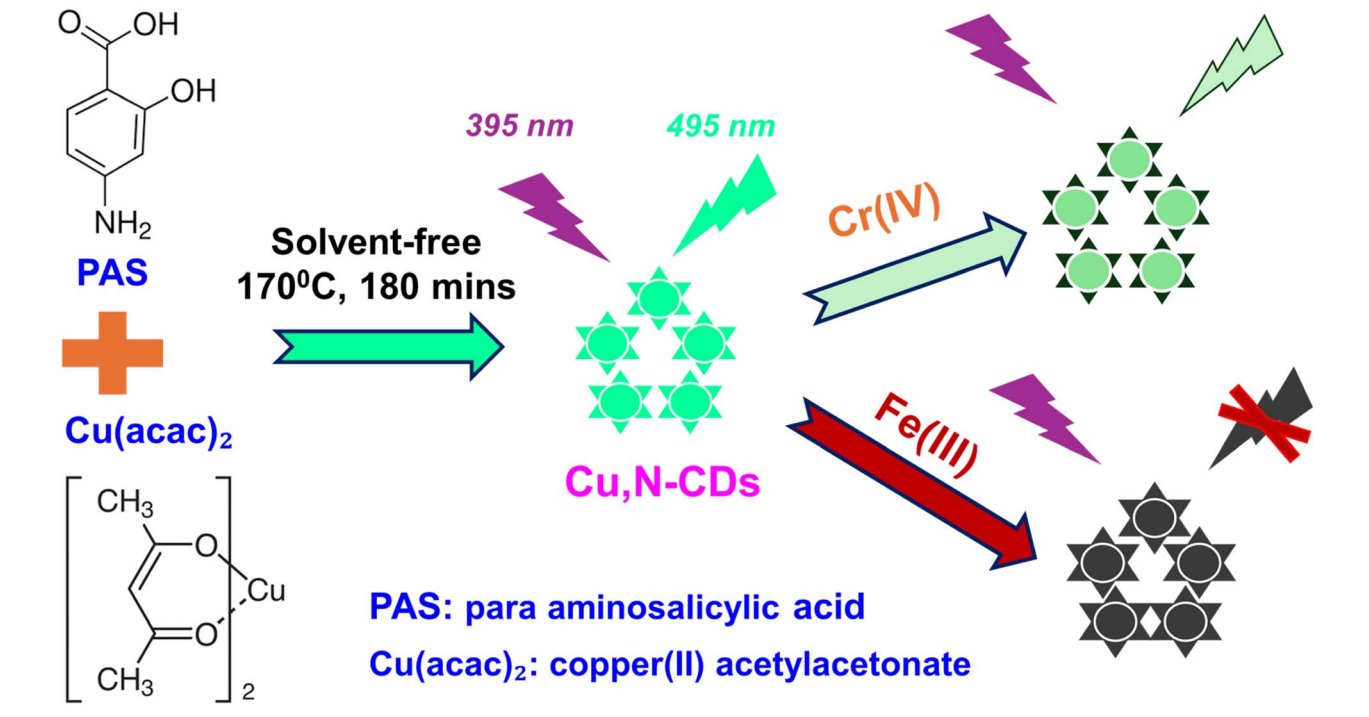

Scheme 1 Solvent-free synthesis of Cu,N-co-doped carbon dots (Cu,N-CDs) and their application as fluorescent probes for the detection of Fe(III) and Cr(VI) ions.

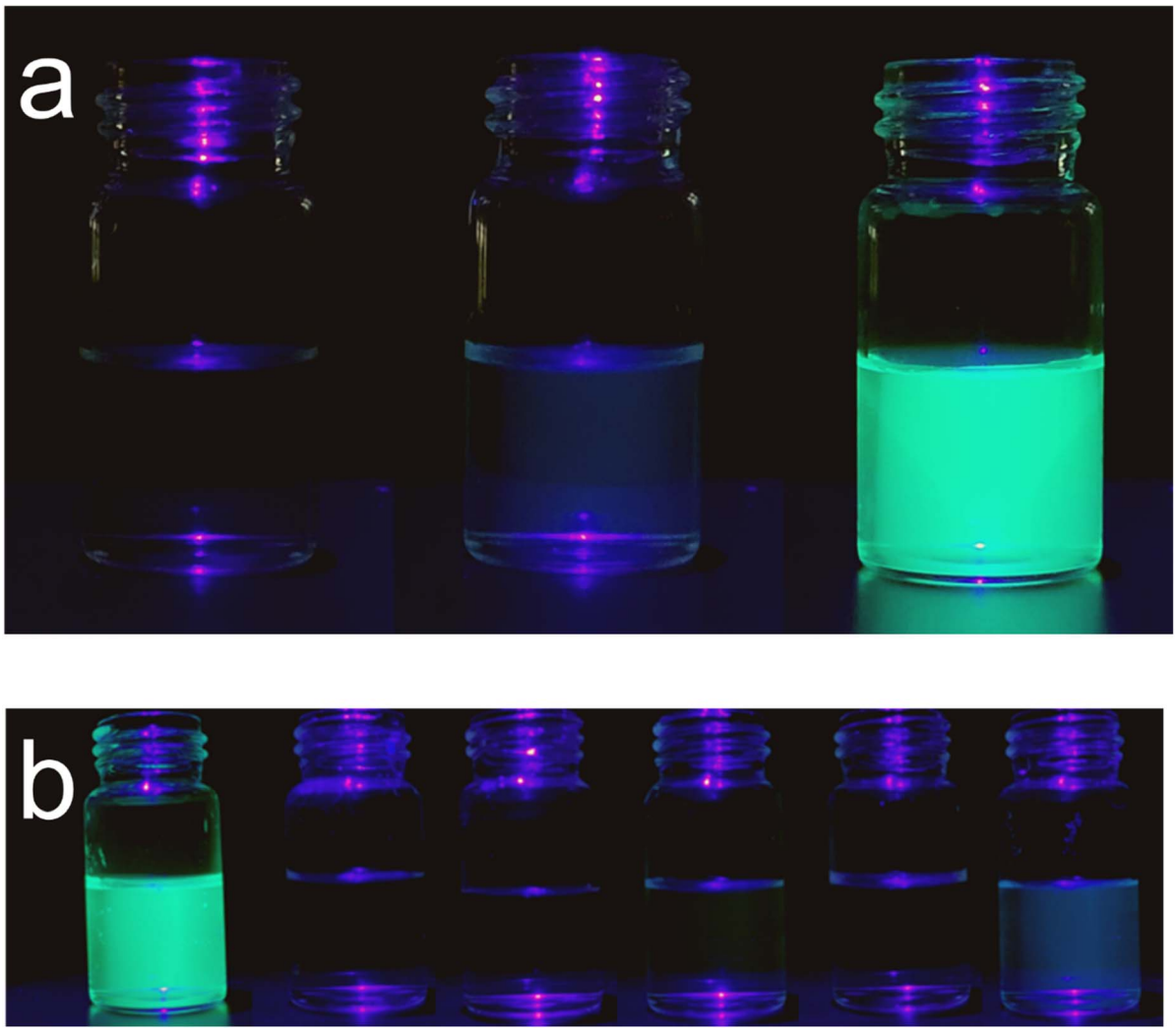

Fig. 1 (a) Digital images of the products following thermal treatment are shown: (left) pure $Cu(acac)_2$, (middle) pure PAS, and (right) a mixture of both precursors. The pyrolysis was conducted at 170 °C for 3 hours, (b) products of reaction between different precursors with $Cu(acac)_2$, from left to right: PAS, salicylic acid, phthalic acid, citric acid, tartaric acid, glutamic acid. All images were captured under 395 nm UV light.

Table 1 Fluorescence outcomes of different precursors pyrolyzed in the presence of $Cu(acac)_2$

Precursor	Aromatic ring	–COOH	–OH	$–NH_2$	Fluorescence
PAS	Yes	Yes	Yes	Yes	Strong green
Salicylic acid	Yes	Yes	Yes	No	None
Phthalic acid	Yes	Yes	No	No	None
Citric acid	No	Yes	Yes	No	None
Tartaric acid	No	Yes	Yes	No	None
Glutamic acid	No	Yes	No	Yes	Weak green

using PAS precursors, which typically yield particles in the range of 5–10 nm (ref. 34) and 3.5–8.5 nm.[32]

Moreover, HRTEM analysis highlights the crystalline nature of the Cu,N-CDs. Distinct lattice fringes with a spacing of 0.32 nm were observed, in excellent agreement with the in-plane lattice spacing of graphene corresponding to the (002) planes of sp^2 graphitic carbon. This finding corroborates earlier studies on carbon-based nanostructures,[35,36] and underscores the successful incorporation of graphitic domains within the Cu,N-CDs.

3.2.2. DLS analysis. The size distribution of the synthesized Cu,N-CDs was further evaluated using dynamic light scattering (DLS), as shown in Fig. 3a. The average hydrodynamic diameter was determined to be 25.1 nm, notably larger than the value obtained from TEM analysis (9.13 nm). TEM images the dry, dehydrated carbon core under high-vacuum conditions. The measured diameter (9.13 ± 2.61 nm) therefore reflects only the hard particle core. DLS, in contrast, measures the hydrodynamic diameter—the diameter of an equivalent sphere diffusing at the same rate in solution under Stokes–Einstein conditions.[37] The hydrodynamic diameter (25.1 ± 0.5 nm) encompasses: (i) the carbon core; (ii) the layer of surface functional groups (–COOH, –OH, $–NH_2$) extending ~1–3 nm into solution; (iii) a hydrogen-bonded hydration shell (contributing

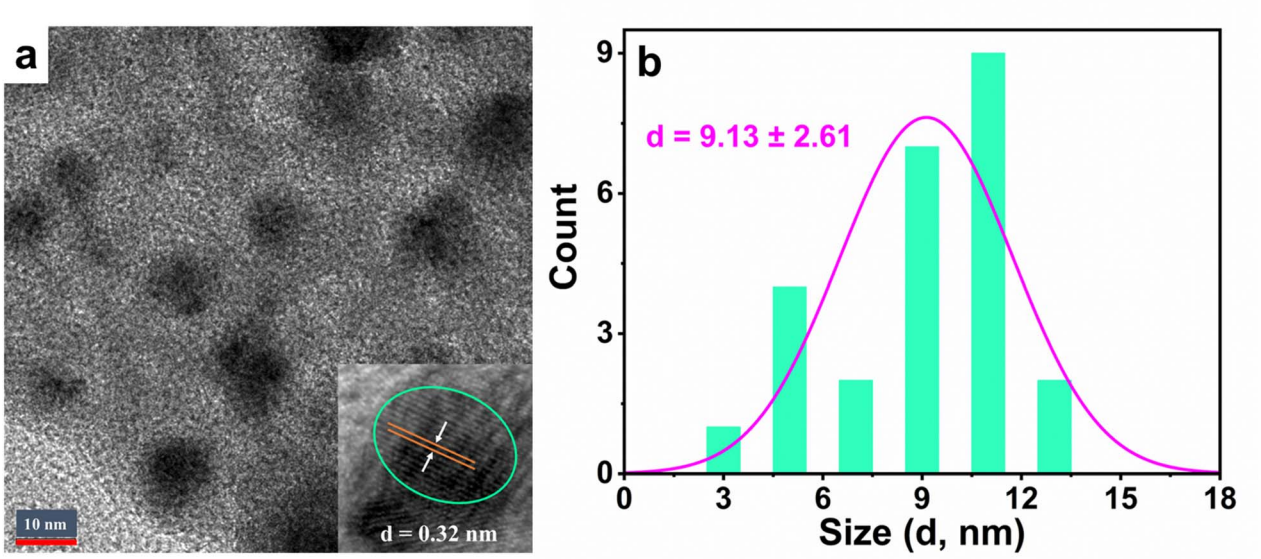

Fig. 2 TEM images of Cu,N-CDs are presented. (a) displays Cu,N-CDs at low resolution, with the inset showing a high-resolution image where crystalline lattices are visible. (b) Illustrates the histogram depicting the particle size distribution of the Cu,N-CDs.

~2–5 nm additional diameter); and (iv) the electrical double layer (Stern and diffuse layers), which is particularly substantial for the negatively charged Cu,N-CDs at low ionic strength. Additionally, DLS intensity-weighting, which is exponentially proportional to radius—r^6,[37] amplifies the apparent contribution of any larger particles or small aggregates present at low concentrations in solution but absent on TEM grids (dried during preparation).[38] The difference between TEM particle size and DLS hydrodynamic size is from the solvation of Cu,N-CDs by water molecules due to high number of hydrophilic functional groups on the surface. Thus, the difference is not from self-aggregation, and this difference should not affect the performance of Cu,N-CDs in sensing applications, particularly in water.

The zeta potential profile, presented in Fig. 3b, exhibits a single peak at −16.84 mV, confirming the presence of negatively charged moieties on the surface of Cu,N-CDs. These surface charges are critical for maintaining electrostatic repulsion between particles, thereby preventing aggregation and enabling stable dispersion in water-based solvents.[39] It should be noted that the zeta potential of −16.84 ± 0.06 mV falls in the 'incipient instability' range (±10–30 mV) based purely on classical electrostatic repulsion of Derjaguin–Landau–Verwey–Overbeek (DLVO) theory. However, colloidal stability is maintained through an additional steric stabilisation mechanism: the surface –COOH and –OH groups extend into the aqueous medium, forming a hydration shell that provides steric/hydration repulsion beyond what the zeta potential alone

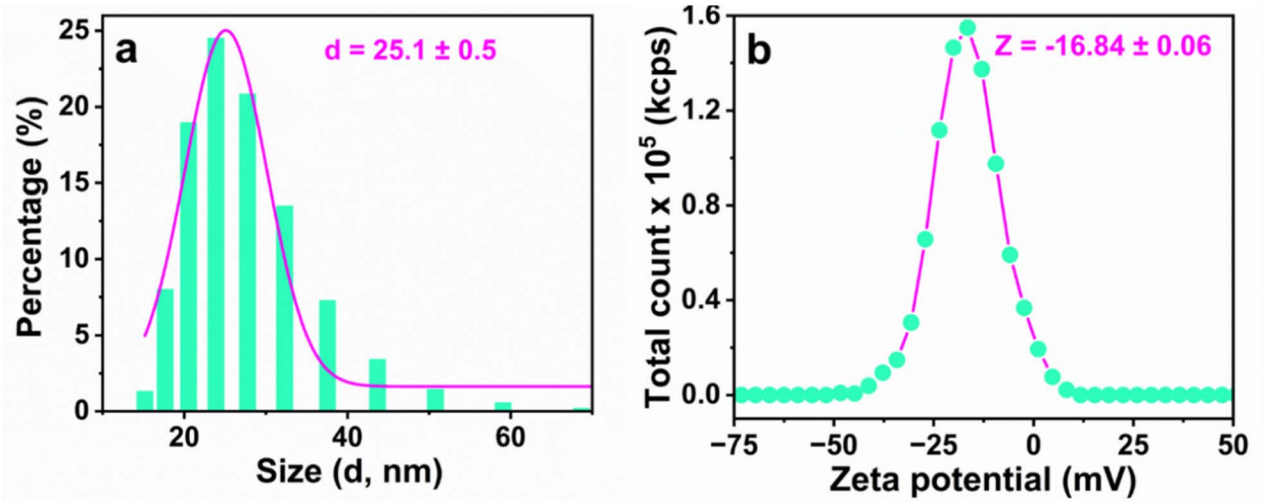

Fig. 3 DLS analysis of Cu,N-CDs: (a) particle size distribution and (b) zeta potential measurements of the synthesized Cu,N-CDs.

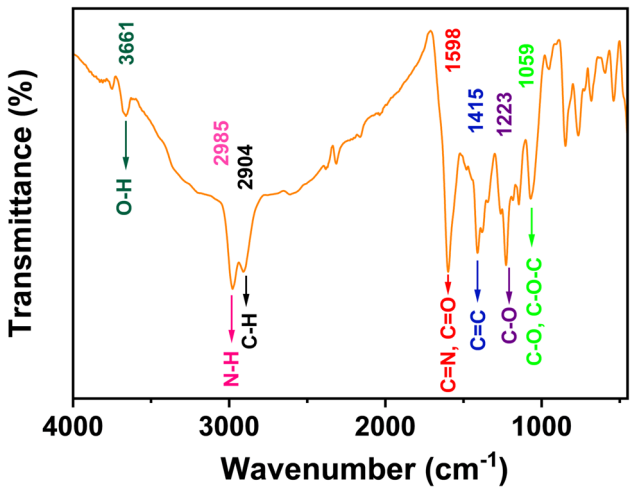

Fig. 4 Fourier-transform infrared (FT-IR) spectra of the Cu,N-CDs.

predicts. In conclusion, the DLS and zeta potential analyses highlight the importance of surface chemistry in governing the colloidal behavior of Cu,N-CDs, reinforcing the role of functional groups in both stability and aqueous compatibility.

3.2.3. FT-IR analysis. FT-IR spectroscopy was employed to probe the surface functional groups of the synthesized Cu,N-CDs, as shown in Fig. 4. Comparable spectral features have been reported in earlier studies.[40,41] Distinct O–H and N–H stretching vibrations at 3661 cm^{-1} and 2985 cm^{-1} confirm the presence of hydroxyl and amino groups, which account for the pronounced hydrophilicity of the Cu,N-CDs.[36,42] The presence of the carboxylic group was confirmed by characteristic absorption bands of O–H (3661 cm^{-1}), the stretching vibration band of C=O, C=N (1598 cm^{-1}) and the stretching vibration bands of C–O (1059 cm^{-1}).[43] The stretching vibrations of aliphatic C–H, C=C were measured at 2904, and 1415 cm^{-1}, respectively, suggesting the presence of alkyl and aryl groups.[44]

The FT-IR analysis verifies the incorporation of diverse oxygen- and nitrogen-containing groups into the Cu,N-CDs, confirming both surface functionalization and nitrogen doping within the carbon core. These features are critical for enhancing dispersion in polar solvents, modulating electronic states, and ultimately governing the photoluminescence behavior of the Cu,N-CDs.

3.2.4. XPS analysis. The elemental composition and surface functionalities of the Cu,N-CDs were probed by X-ray

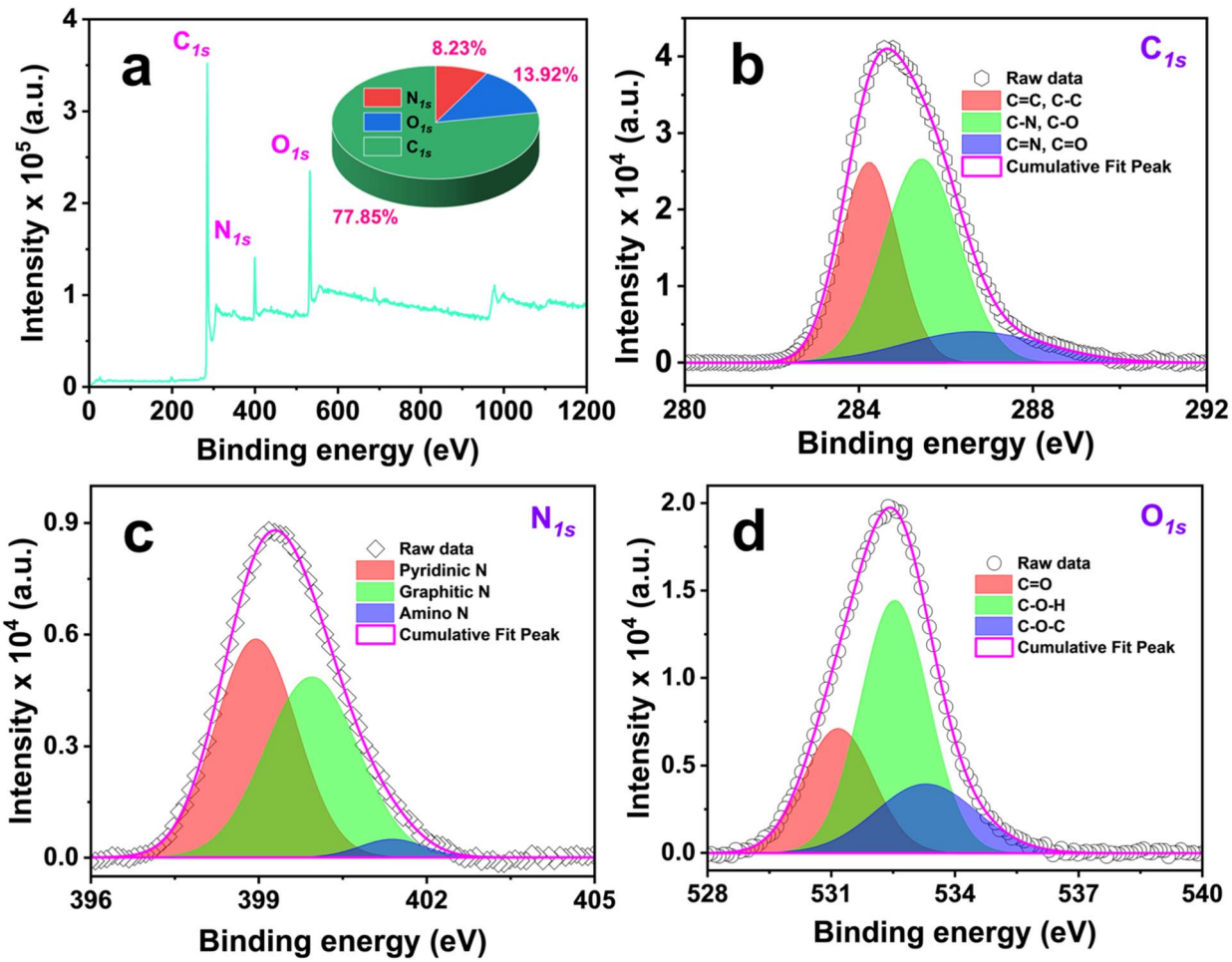

Fig. 5 XPS analysis of Cu,N-CDs samples is presented. (a) displays the XPS survey spectrum, while (b–d) illustrate the deconvoluted high-resolution spectra for C_{1s}, N_{1s}, and O_{1s} peaks, respectively.

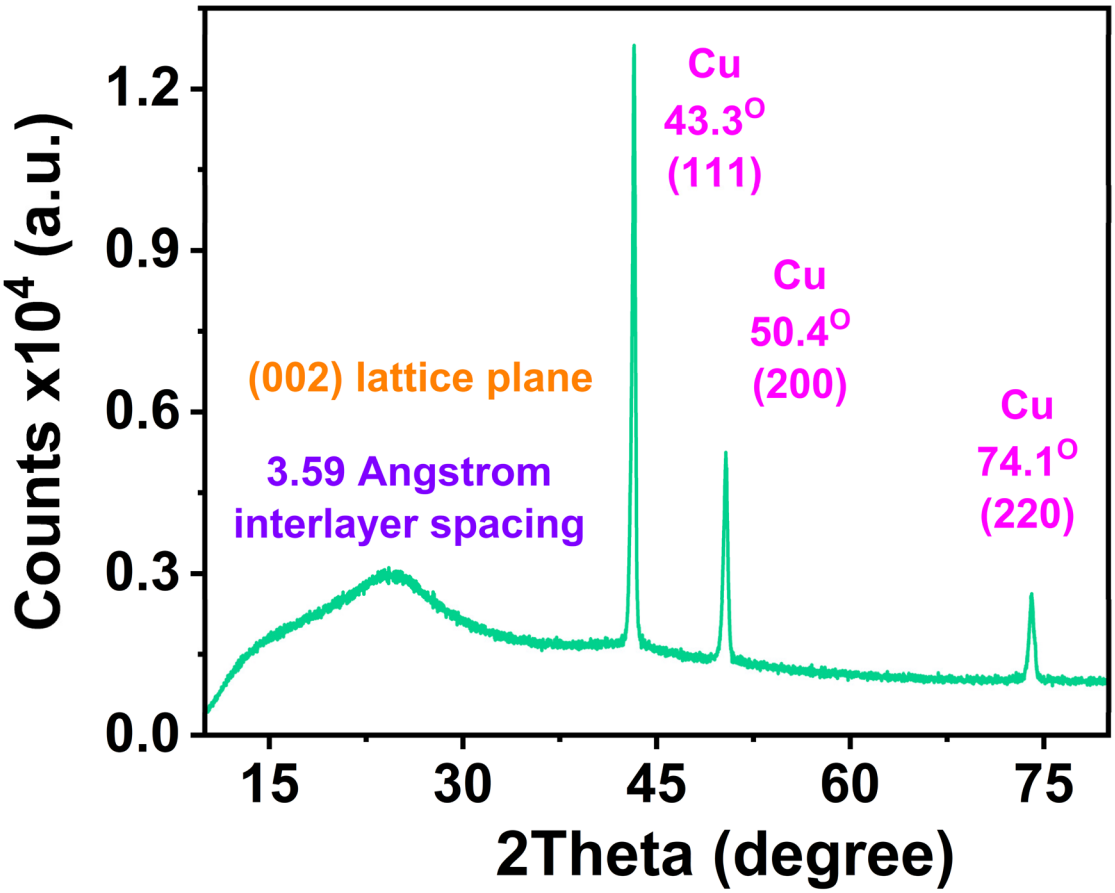

Fig. 6 XRD analysis of Cu,N-CDs samples.

photoelectron spectroscopy (XPS). Fig. 5a shows three dominant peaks at 532.8, 400.8, and 285.8 eV, corresponding to O_{1s}, N_{1s}, and C_{1s}, respectively.[45] The pronounced N_{1s} signal confirms the effective interaction between copper(II) acetylacetonate and *para*-aminosalicylic acid, thereby validating the successful synthesis of nitrogen-doped CDs.

High-resolution spectra (Fig. 5b–d) provide further insight into the chemical states of the constituent elements. The C_{1s}

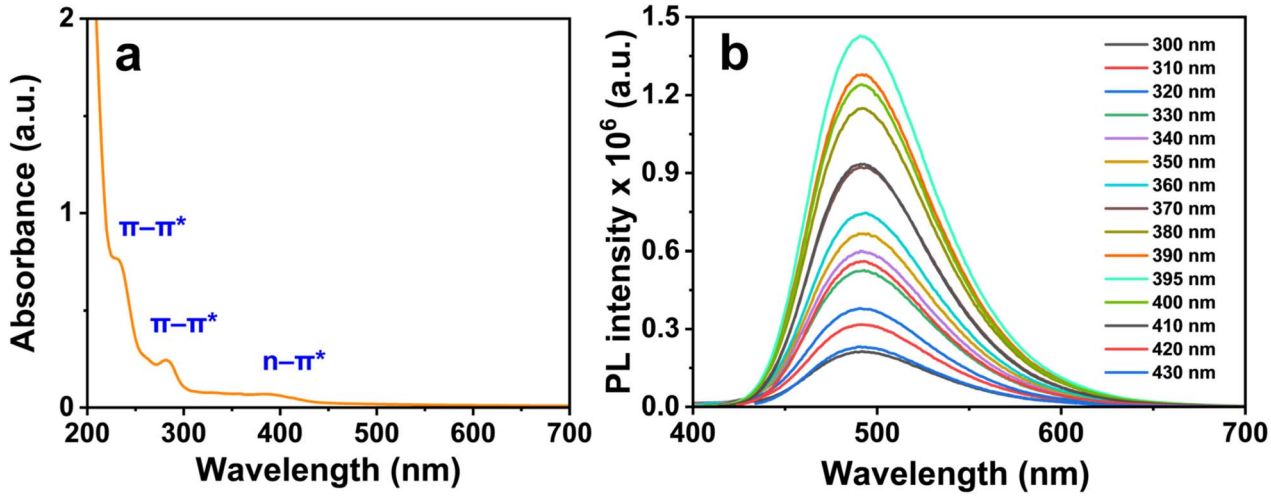

Fig. 7 Optical characteristics of the Cu,N-CDs sample are presented as follows: (a) ultraviolet-visible absorption spectra and (b) photoluminescence emission spectra measured for the Cu,N-CDs across different excitation wavelengths. All measurements were conducted with samples containing Cu,N-CDs diluted to a concentration of 4.8 μg mL^{-1}.

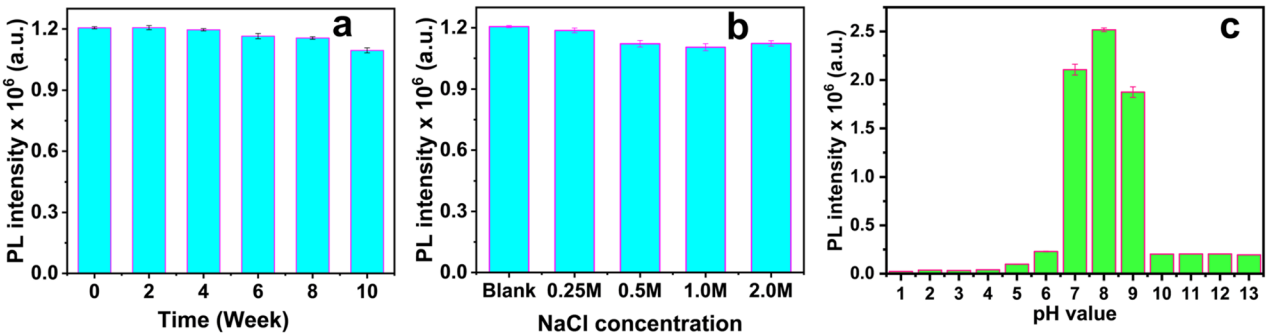

Fig. 8 Stability of Cu,N-CDs with regard to (a) time, (b) ionic strength, and (c) pH. All measurements were conducted with samples containing Cu,N-CDs diluted to a concentration of 4.8 μg mL^{-1}.

spectrum (Fig. 5b) can be deconvoluted into three peaks at 284.2, 285.4, and 286.7 eV, assigned to C–C/C=C, C–N/C–O, and C=O groups, respectively. The N_{1s} spectrum (Fig. 5c) reveals contributions from pyridinic-like nitrogen (398.95 eV), graphitic-like nitrogen (399.95 eV), and amino nitrogen (401.4 eV).[46] The O_{1s} spectrum (Fig. 5d) exhibits peaks at 531.2, 532.5, and 533.6 eV, corresponding to C=O, C–O–H, and C–O–C groups, respectively.[47]

Collectively, these XPS results demonstrate the incorporation of nitrogen into both the carbon core (pyridinic and graphitic N) and the surface (amino groups), alongside oxygen-containing functionalities. Graphitic N can produce electron-doping effect by donating electron to the HOMO–LUMO gap, causing strong red-shift in absorption spectra of CDs.[48] Such structural features are critical for modulating electronic states, enhancing surface defect emission, and ultimately driving the pronounced photoluminescence (PL) of the Cu,N-CDs.

3.2.5. XRD analysis. The XRD pattern of the Cu,N-CDs (Fig. 6) displays a broad diffraction peak at $2\theta = 24.78°$, corresponding to the (002) reflection of graphitic/amorphous carbon with a calculated *d*-spacing of 0.358 nm. This value is slightly larger than the standard graphene interlayer spacing (0.34 nm), and the peak broadening is indicative of a moderately graphitized, partially amorphous carbon phase consistent with the role of the PAS aromatic nucleus in nucleating sp^2 domains. Additional diffraction features in the XRD pattern are attributable to metallic Cu incorporated within the carbon matrix.

The absence of Cu signals in the XPS spectra, in contrast to the XRD data, is expected when the limitations of XPS are considered. XPS is inherently surface-sensitive, with an analytical depth of only ~5–10 nm,[49] so if Cu atoms are buried within the carbon matrix, they are inaccessible to the photoelectron signal. If Cu atoms were present on the particle surface, they would be immediately oxidized during aqueous purification, and copper oxide phases rather than metallic Cu would appear in the XRD pattern. This interpretation is further supported by the work of Fu *et al.*,[50] who demonstrated that upon carbonization of Cu-doped carbon aerogels, Cu ions are reduced to metallic nanoparticles that migrate into the carbon matrix, become coated by a thin carbon layer, and are consequently

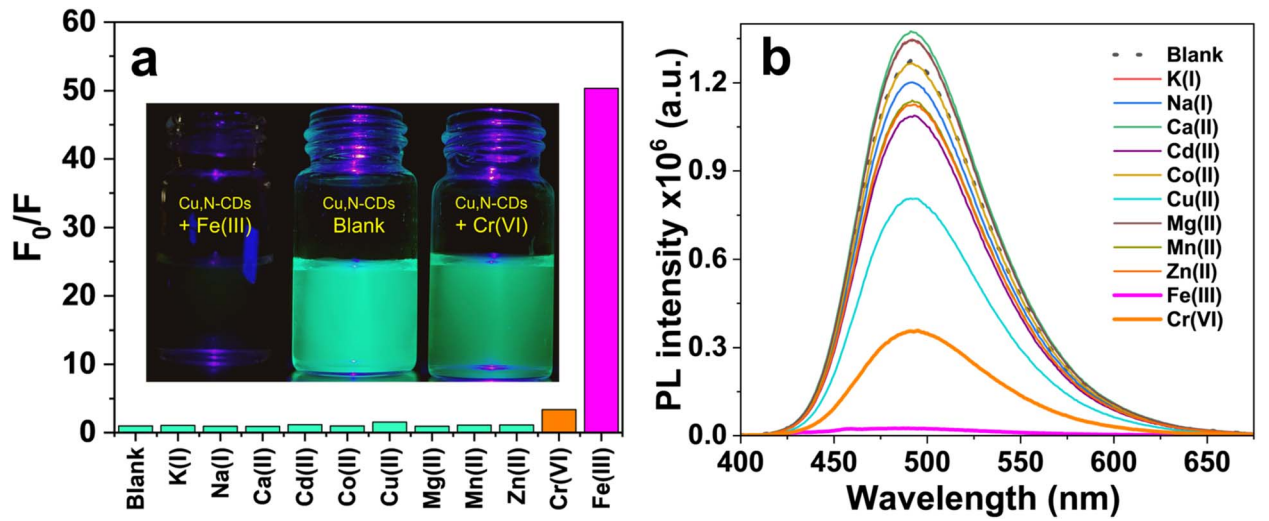

Fig. 9 Effect of quenchers (Fe(III) and Cr(VI)) on Cu,N-CDs from the results of: (a) fluorescence enhancement factors (F_0/F) and digital images, (b) photoluminescence (PL) emission spectra. The concentrations of Cu,N-CDs and metal ions were maintained at 4.8 μg mL^{-1} and 100 μM, respectively.

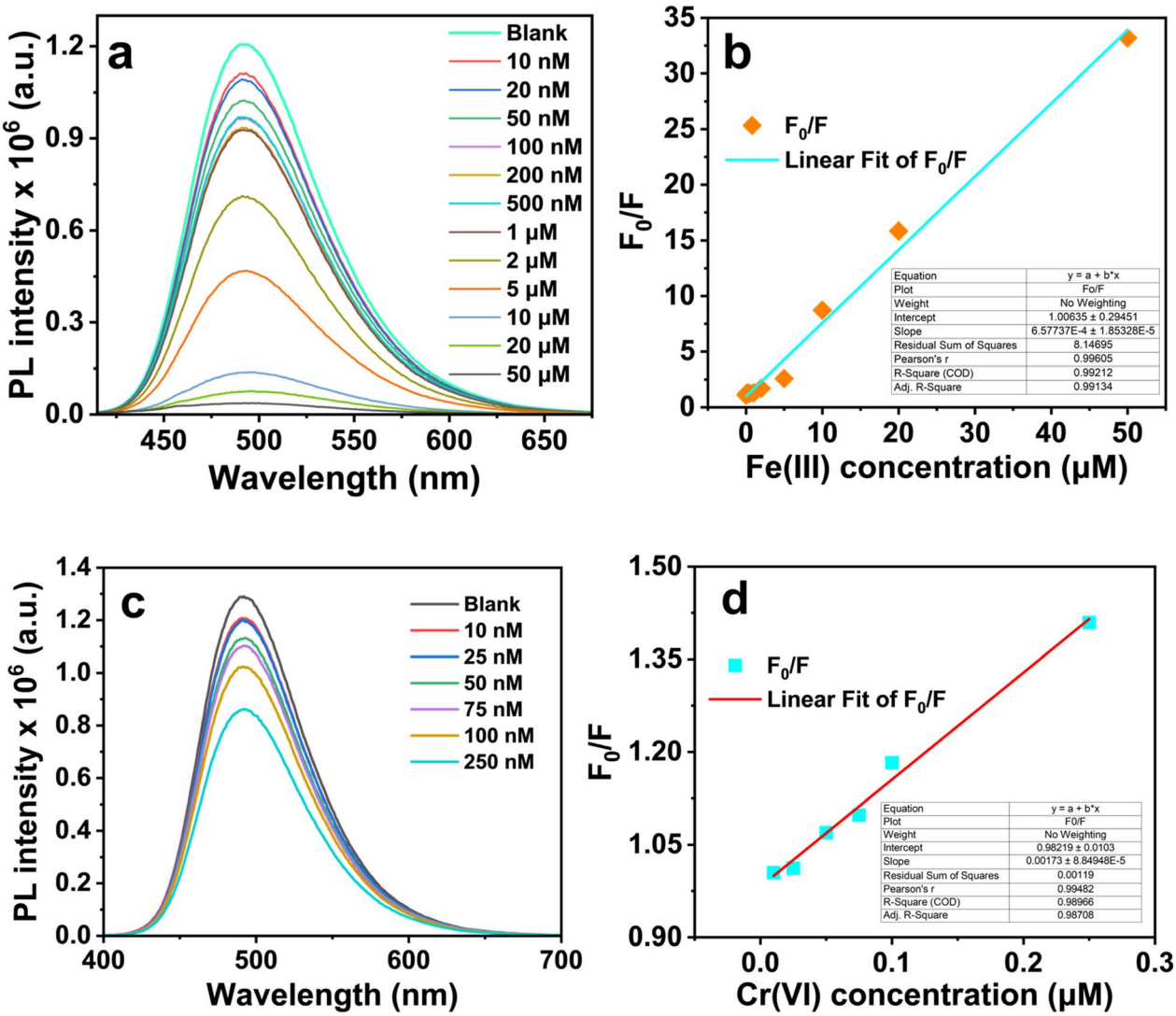

Fig. 10 (a) PL response of Cu,N-CDs with increasing Fe(III) ion concentrations ranging from 10 nM to 50 μM, (b) plot of F_0/F *versus* Fe(III) concentration, (c) PL response of Cu,N-CDs with increasing Cr(VI) ion concentrations ranging from 10 nM to 250 nM, (d) plot of F_0/F *versus* Cr(VI) concentration. PL measurements were conducted at an excitation wavelength of 395 nm with samples containing Cu,N-CDs diluted to a concentration of 4.8 μg mL^{-1}.

undetectable by XPS. Another possible reason for non-detecting Cu in XPS spectra is due to the low Cu content (~0.88 at% by EDX, Fig. S1 and Table S4, SI), which falls near the typical XPS detection threshold (~0.1–1.0 at%).[51]

Based on these characterization data, $Cu(acac)_2$ is cautiously proposed to fulfil three sequential roles during Cu,N-CDs formation. As a structural facilitator, it melts and decomposes at the pyrolysis temperature, being reduced by PAS to generate *in situ* Cu nanoparticles. As a catalyst, the freshly formed, highly reactive Cu nanoparticles promote condensation and coupling reactions among PAS molecules and acetylacetonate fragments, extending the conjugated π system and facilitating carbonization at the mild temperature of 170 °C. As a dopant, Cu atoms are progressively encapsulated by the growing aromatic carbon layer, protecting the metallic Cu core from oxidation and modulating the electronic structure of the Cu,N-CDs.

3.2.6. Optical analysis. The optical characteristics of the Cu,N-CDs were investigated using UV-Vis absorption and photoluminescence (PL) spectroscopy. As shown in Fig. 7a, the UV-Vis spectrum of the Cu,N-CDs solution displays a distinct shoulder near 235 nm and a pronounced peak at 285 nm, both of which are attributed to π–π* transitions within aromatic sp^2 domains originating from the carbon core. In addition, a broad absorption shoulder centered around 395 nm is observed, corresponding to n–π* transitions associated with surface functional groups. Notably, this absorption feature coincides with the maximum PL emission peak under excitation at 395 nm, suggesting the coupling between core electronic states and surface functionalities in governing the optical response of the Cu,N-CDs.

Fig. 7b presents the PL spectra at varying excitation wavelengths. A maximum emission at 495 nm (green emission) was

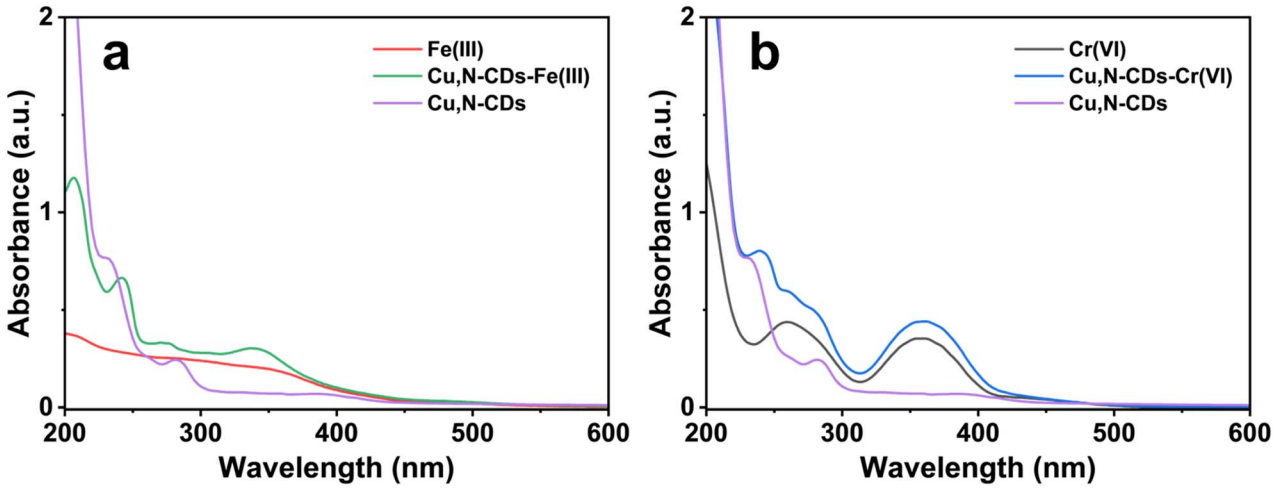

Fig. 11 Investigating quenching mechanisms from UV-Vis spectroscopy for Fe(III) (a) and Cr(VI) (b). The concentration of both quenchers are 100 μM. Blank sample containing Cu,N-CDs diluted to a concentration of 4.8 μg mL^{-1}.

observed under excitation at 395 nm, and the emission peak position remained constant as the excitation wavelength was varied from 300 to 430 nm, demonstrating excitation-independent emission behavior. This behavior has previously been attributed to uniform particle size and surface state distributions,[52] or to the passivation of surface traps by functional groups.[53] In the present system, however, the weak visible-region absorption of surface groups (Fig. 7a) suggests that surface state contributions are limited. We therefore propose that the excitation-independent emission arises primarily from heteroatom doping of the carbon core, consistent with the findings of Azami *et al.*,[54] who demonstrated that core-embedded heteroatom doping fundamentally alters the optical behavior of CDs.

Based on these characterization results, the following structure–property relationships are proposed cautiously. The optical emission of the Cu,N-CDs arises primarily from π–π* transitions of the conjugated sp^2 carbon core, modulated by both nitrogen incorporation and Cu doping. Nitrogen atoms increase the electron density of the π system, consistent with the observed green emission at 495 nm—red-shifted relative to the blue emission (~430–460 nm) typical of undoped or lightly doped CDs. Cu incorporation may further perturb the π–electron distribution, potentially narrowing the π–π* energy gap and contributing to the red shift and fluorescence enhancement.[55] Since XPS and FT-IR did not reveal unambiguous evidence of direct Cu–N or Cu–O coordination bonds, a definitive mechanistic assignment is not possible at this stage. Further spectroscopic investigation, such as extended X-ray absorption fine structure (EXAFS) analysis, would be required to fully resolve the Cu–carbon interaction.

The quantum yield (QY) of the Cu,N-CDs was determined using the relative method, with quinine sulfate serving as a standard reference dye (Table S2, SI). A QY as high as 14.9% was achieved, a value that is comparable to or surpasses those reported for nitrogen-doped CDs synthesized *via* alternative routes (Table S3, SI). This result highlights the efficiency of the present solvent-free pyrolytic approach, demonstrating that high-performance Cu,N-CDs can be obtained through a simple and scalable synthesis strategy.

3.3. Colloidal and storage stability, and effect of pH

The fluorescence intensity of the Cu,N-CDs showed no significant decrease (<5%) after storage at room temperature for 10 weeks (Fig. 8a), and remained unchanged in NaCl solutions up to 2 M (Fig. 8b), demonstrating excellent long-term storage and ionic strength stability suitable for practical sensing applications.

The effect of pH on the PL intensity of the Cu,N-CDs was also investigated (Fig. 8c). Maximum fluorescence intensity was observed in the pH range of 7–9, with quenching observed outside this window. All subsequent sensing experiments were therefore conducted in deionized water to ensure optimal and stable fluorescence response.

3.4. Applications of Cu,N-CDs as fluorescent probe for Fe(III) and Cr(VI) ions

To evaluate their specificity toward Fe(III) and Cr(VI) ions, the PL intensity at 495 nm was measured in the presence of various competing metal ions [K(I), Na(I), Ca(II), Cd(II), Co(II), Cu(II), Mg(II), Mn(II), Zn(II)] at concentrations of 100 μM. Among these, Fe(III) and Cr(VI) induced the most pronounced quenching of PL intensity: quenching factor are 50.3 and 3.53 (Fig. 9a), respectively, whereas other ions produced negligible or minimal effects. A sharp reduction in fluorescence was observed immediately upon mixing either Fe(III) or Cr(VI) with the Cu,N-CDs solution, as can be seen from the digital images in Fig. 9a.

The sensitivity of Cu,N-CDs for both Fe(III) and Cr(VI) was evaluated by adding different concentrations of Fe(III) and Cr(VI) into Cu,N-CDs solution, and the corresponding fluorescence response was recorded. Relative fluorescence intensity (F_0/F) of Cu,N-CDs linearly decreased by increasing Fe(III) in the range of 0.01–50 μM. For Cr(VI), a good linearity was also observed in the

range of: 0.01–0.25 μM. This behavior could be described by the Stern–Volmer equation ($F_0/F = K_{sv}[C] + 1$), where F_0 and F are the fluorescence intensities recorded in absence and presence of quencher, respectively, $[C]$ is the concentration of quencher and K_{sv} is the Stern–Volmer quenching constant. The high K_{sv} shows high affinity of Cu,N-CDs towards Fe(III) and Cr(VI).

$$F_0/F = 6.58 \times 10^5 \times C_{Fe(III)} + 1 \ (R^2 = 0.99)$$

$$F_0/F = 1.73 \times 10^6 \times C_{Cr(VI)} + 0.98 \ (R^2 = 0.99)$$

The lowest detection concentrations (LOD) of Fe(III) and Cr(VI) were about 1.48 μM and 19.6 nM, respectively (Tables S5 and S6, SI). These values underscore the high sensitivity of the Cu,N-CDs and their ability to detect Fe(III) and Cr(VI) ions at low concentrations. These results highlight the strong potential of Cu,N-CDs as efficient fluorescent probes for Fe(III) and Cr(VI) sensing in aqueous environments, combining selectivity with a low detection threshold (Fig. 10).

The sensing performance of the Cu,N-CDs was benchmarked against recently reported CD-based fluorescent probes for Fe(III) and Cr(VI), summarized in Table S7 (SI). For Fe(III) detection, the LOD of 1.48 μM achieved by the Cu,N-CDs is comparable to the majority of hydrothermal N-CD systems (0.0138–3.8 μM range), while the solvent-free pyrolysis route offers a distinct synthetic advantage in avoiding high-pressure autoclaves and toxic solvents. For Cr(VI) detection, the LOD of 19.6 nM achieved by the Cu,N-CDs is among the lowest reported for CD-based Cr(VI) sensors. Notably, this work is, to our knowledge, the first report of a solvent-free pyrolysis-derived CD system capable of simultaneous dual detection of both Fe(III) and Cr(VI), which distinguishes it from the single-analyte systems that comprise the majority of the literature.

The quenching mechanisms can be interpreted from UV-Vis spectroscopy (Fig. 11). The UV-Vis spectrum of the Cu,N-CD solution after addition of Fe(III) reveals a new absorption feature at approximately 340 nm that is absent in either the Cu,N-CDs solution or the Fe(III) solution alone. This peak is consistent with a ligand-to-metal charge transfer (LMCT) band arising from coordination of surface α-hydroxycarboxylate and amine groups to Fe(III), forming a non-fluorescent ground-state complex.[56] This represents static quenching, in which the fluorescent population is depleted by sequestration of Cu,N-CDs into non-emissive complexes without altering the excited-state lifetime of the remaining free Cu,N-CDs. Additionally, Fe(III) displays strong UV absorption in the 300–400 nm region in aqueous solution, overlapping with the Cu,N-CDs excitation wavelength at 395 nm, contributing an inner filter effect (IFE) component. The exceptionally strong quenching factor (F_0/F = 50.3 at 100 μM) thus reflects the synergistic operation of coordination-induced static quenching and IFE.

Unlike Fe(III), Cr(VI) exists as oxyanions (CrO_4^{2-}, $Cr_2O_7^{2-}$) at neutral pH and does not form classical LMCT-type coordination complexes with surface donor groups. No new absorption feature was observed in the UV-Vis spectrum of the mixture of Cr(VI) and Cu,N-CDs, in contrast to the Fe(III) case, suggesting the absence of a strong ground-state coordination complex. The quenching by Cr(VI) is therefore attributed primarily to IFE: the absorption bands of Cr(VI) (250–400 nm) overlap with the Cu,N-CDs excitation wavelength (395 nm), reducing the excitation light reaching the fluorophores. The lower quenching factor ($F_0/F = 3.53$ *vs.* 50.3 at 100 μM) is consistent with the absence of an LMCT contribution and the weaker UV absorption of Cr(VI) near 395 nm. The difference in quenching factor between Fe(III) and Cr(VI) are also consistent with the zeta potential of Cu,N-CDs. For Fe^{3+} (trivalent cation), electrostatic attraction concentrates the analyte near the Cu,N-CDs surface, facilitating coordination complex formation. For Cr(VI) (existing as $Cr_2O_7^{2-}$ anions at neutral–basic pH), electrostatic repulsion from the negatively charged surface precludes surface contact. The quenching mechanism is therefore entirely optical (IFE)—no physical approach to the Cu,N-CDs surface is required.

4. Conclusions

This work introduces a facile, solvent-free strategy for the synthesis of fluorescent Cu,N-codoped carbon dots (Cu,N-CDs) through thermal treatment of a solid mixture comprising *p*-aminosalicylic acid and copper(II) acetylacetonate. Cu,N-CDs formation was not achieved when either precursor was used independently; however, their combination markedly promoted successful synthesis through a proposed three-stage mechanism involving Cu nanoparticle formation, Cu-catalyzed condensation of the aromatic precursor, and encapsulation of metallic Cu within the growing carbon shell. The resulting Cu,N-CDs exhibit intense green photoluminescence with a quantum yield of 14.9%, excellent colloidal stability under ambient conditions. Beyond their optical properties, the Cu,N-CDs function as efficient, label-free fluorescent probes for the selective and sensitive simultaneous detection of Fe(III) and Cr(VI) ions, achieving limits of detection of 1.48 μM and 19.6 nM, respectively. The Cr(VI) LOD of 19.6 nM is among the lowest reported for CD-based Cr(VI) sensors. These findings establish that high-performance fluorescent nanosensors are achievable by strategic solvent-free pyrolysis of functional aromatic compounds, offering a scalable, green, and practical route to dual-analyte sensing platforms with applications in environmental water monitoring and food safety screening.

Author contributions

Thien-Phuc Nguyen: investigation, formal analysis, writing – original draft, project administration. Thu Nhu Vo Thi: writing – review and editing, Minh Hao Hoang: methodology, software. Nham Linh Nguyen: writing – review and editing. Thanh-Sang Nguyen: visualization, writing – review and editing. Dat Nguyen: formal analysis, investigation, writing – review and editing. Nhiem Ly: formal analysis, investigation, writing – review and editing. Phuong V. Pham: data curation, formal analysis, investigation. Thanh Tuyen Nguyen: data curation, Dinh Khoi Dang: supervision, funding acquisition, conceptualization, writing – original draft.

Conflicts of interest

There are no conflicts to declare.

Data availability

The data supporting this article are included in the supplementary information (SI). Supplementary information is available. See DOI: https://doi.org/10.1039/d6ra00625f.

Acknowledgements

This study is funded by the Ho Chi Minh City University of Technology and Engineering with the reference number T2025-92.

References

1 F. Lemessa, B. Simane, A. Seyoum and G. Gebresenbet, Analysis of the concentration of heavy metals in soil, vegetables and water around the bole Lemi industry park, Ethiopia, *Heliyon*, 2022, **8**(12), e12429, DOI: 10.1016/j.heliyon.2022.e12429.

2 D. Ellis, C. Bouchard and G. Lantagne, Removal of iron and manganese from groundwater by oxidation and microfiltration, *Desalination*, 2000, **130**(3), 255–264, DOI: 10.1016/S0011-9164(00)00090-4.

3 L. S. Chawla, B. Beers-Mulroy and G. F. Tidmarsh, Therapeutic opportunities for hepcidin in acute care medicine, *Crit. Care Clin.*, 2019, **35**(2), 357–374, DOI: 10.1016/j.ccc.2018.11.014.

4 S. Puntarulo, Iron, oxidative stress and human health, *Mol. Aspects Med.*, 2005, **26**(4–5), 299–312, DOI: 10.1016/j.mam.2005.07.001.

5 S. He, S. Chen, L. Zhang, S. Tan, H. Wen, L. Xi, *et al.*, Dissolved humic substances-mediated electron shuttling unlocking nanoscale zero-valent iron reactivity in shewanella oneidensis MR-1 systems for enhanced Cr(VI) removal, *Chem. Eng. J.*, 2025, **520**, 166048, DOI: 10.1016/j.cej.2025.166048.

6 World Health Organization, Chemical fact sheets: Chromium, [cited 2025 Nov 30]. Available from: https://www.who.int/publications/m/item/chemical-fact-sheets–chromium.

7 M. Costa, Toxicity and carcinogenicity of Cr(VI) in animal models and humans, *Crit. Rev. Toxicol.*, 1997, **27**(5), 431–442, DOI: 10.3109/10408449709078442.

8 T. L. DesMarias and M. Costa, Mechanisms of chromium-induced toxicity, *Curr. Opin. Toxicol.*, 2019, **14**, 1–7, DOI: 10.1016/j.cotox.2019.05.003.

9 H. Hossini, B. Shafie, A. D. Niri, M. Nazari, A. J. Esfahlan, M. Ahmadpour, *et al.*, A comprehensive review on human health effects of chromium: insights on induced toxicity, *Environ. Sci. Pollut. Res.*, 2022, **29**(47), 70686–70705, DOI: 10.1007/s11356-022-22705-6.

10 S. F. Sulthana, U. M. Iqbal, S. B. Suseela, R. Anbazhagan, R. Chinthaginjala, D. Chitathuru, *et al.*, Electrochemical sensors for heavy metal ion detection in aqueous medium: a systematic review, *ACS Omega*, 2024, **9**(24), 25493–25512, DOI: 10.1021/acsomega.4c00933.

11 M. Nejadmansouri, M. Majdinasab, G. S. Nunes and J. L. Marty, An overview of optical and electrochemical sensors and biosensors for analysis of antioxidants in food during the last 5 years, *Sens*, 2021, **21**(4), 1176, DOI: 10.3390/s21041176.

12 O. Chailapakul, S. Korsrisakul, W. Siangproh and K. Grudpan, Fast and simultaneous detection of heavy metals using a simple and reliable microchip-electrochemistry route: an alternative approach to food analysis, *Talanta*, 2008, **74**(4), 683–689, DOI: 10.1016/j.talanta.2007.06.034.

13 K. Zhang, X. Tian, P. Xu, Y. Zhu, S. Guang and H. Xu, Multi-ion detection chemosensor based on rhodamine for turn-on fluorescence sensing and bioimaging of Fe^{3+}, Al^{3+}, Cr^{3+}, and Hg^{2+} under different channels, *Spectrochim. Acta, Part A*, 2024, **318**, 124484, DOI: 10.1016/j.saa.2024.124484.

14 N. Xin, D. Gao, B. Su, T. Zhou, Y. Zhu, C. Wu, *et al.*, Orange-emissive carbon dots with high photostability for mitochondrial dynamics tracking in living cells, *ACS Sens.*, 2023, **8**(3), 1161–1172, DOI: 10.1021/acssensors.2c02451.

15 Q. X. Mao, W. J. Wang, X. Hai, Y. Shu, X. W. Chen and J. H. Wang, The regulation of hydrophilicity and hydrophobicity of carbon dots via a one-pot approach, *J. Mater. Chem. B*, 2015, **3**(29), 6013–6018, DOI: 10.1039/C5TB00963D.

16 M. Zhang, X. Zhao, Z. Fang, Y. Niu, J. Lou, Y. Wu, *et al.*, Fabrication of HA/PEI-functionalized carbon dots for tumor targeting, intracellular imaging and gene delivery, *RSC Adv.*, 2017, **7**(6), 3369–3375, DOI: 10.1039/C6RA26048A.

17 Y. Sun, C. Shen, J. Wang and Y. Lu, Facile synthesis of biocompatible N, S-doped carbon dots for cell imaging and ion detecting, *RSC Adv.*, 2015, **5**(21), 16368–16375, DOI: 10.1039/C4RA13820A.

18 D. Xu, F. Lei, H. Chen, L. Yin, Y. Shi and J. Xie, One-step hydrothermal synthesis and optical properties of self-quenching-resistant carbon dots towards fluorescent ink and as nanosensors for Fe^{3+} detection, *RSC Adv.*, 2019, **9**(15), 8290–8299, DOI: 10.1039/C8RA10570G.

19 Y. Chai, Y. Feng, K. Zhang and J. Li, Preparation of fluorescent carbon dots composites and their potential applications in biomedicine and drug delivery—a review, *Pharmaceutics*, 2022, **14**(11), 2482, DOI: 10.3390/pharmaceutics14112482.

20 S. Sahana, A. Gautam, R. Singh and S. Chandel, A recent update on development, synthesis methods, properties and application of natural products derived carbon dots, *Nat. Prod. Bioprospect.*, 2023, **13**(1), 51, DOI: 10.1007/s13659-023-00415-x.

21 M. Chen, J. Zhai, Y. An, Y. Li, Y. Zheng, H. Tian, *et al.*, Solvent-free pyrolysis strategy for the preparation of biomass carbon dots for the selective detection of Fe^{3+} ions, *Front. Chem.*, 2022, **10**, 940398, DOI: 10.3389/fchem.2022.940398.

22 M. A. P. Martins, C. P. Frizzo, D. N. Moreira, L. Buriol and P. Machado, Solvent-free heterocyclic synthesis, *Chem. Rev.*, 2009, **109**(9), 4140–4182, DOI: 10.1021/cr9001098.

23 Y. Song, C. Zhu, J. Song, H. Li, D. Du and Y. Lin, Drug-derived bright and color-tunable N-doped carbon dots for cell imaging and sensitive detection of Fe^{3+} in living cells, *ACS Appl. Mater. Interfaces*, 2017, **9**(8), 7399–7405, DOI: 10.1021/acsami.6b13954.

24 S. Sudan, J. Kaushal, T. G. Singh, M. H. Mahmoud, A. Alexiou, M. Papadakis, *et al.*, Eco-friendly sensing of hexavalent chromium ions via copper-doped carbon quantum dots: a fluorescent probe for water safety, *Microchim. Acta*, 2025, **192**(2), 88, DOI: 10.1007/s00604-024-06939-4.

25 F. Nichols, J. E. Lu, R. Mercado, M. D. Rojas-Andrade, S. Ning, Z. Azhar, *et al.*, Antibacterial activity of nitrogen-doped carbon dots enhanced by atomic dispersion of copper, *Langmuir*, 2020, **36**(39), 11629–11636, DOI: 10.1021/acs.langmuir.0c02293.

26 Z. Zhang, Y. Zhang, Y. Jiang, W. Pang, H. Gao, Z. Yuan, *et al.*, Effects of carbon dots and their composites on the burning performance of HMX-CMDB propellant, *Def. Technol.*, 2026, **57**, 27–40, DOI: 10.1016/j.dt.2025.10.011.

27 G. Bartholazzi, M. M. Shehata, D. H. Macdonald and L. E. Black, Atomic layer deposition of Cu_2O using copper acetylacetonate, *J. Vac. Sci. Technol., A*, 2023, **41**(2), 022402, DOI: 10.1116/6.0002238.

28 G. Indrayanto, Validation of chromatographic methods of analysis: application for drugs that derived from herbs, in *Profiles of Drug Substances, Excipients and Related Methodology*, Elsevier, 2018, pp. 359–392, DOI: 10.1016/bs.podrm.2018.01.003, Available from: https://linkinghub.elsevier.com/retrieve/pii/S1871512518300037.

29 S. Wang, I. S. Cole, D. Zhao and Q. Li, The dual roles of functional groups in the photoluminescence of graphene quantum dots, *Nanoscale*, 2016, **8**(14), 7449–7458, DOI: 10.1039/C5NR07042B.

30 Z. Wei, W. Lu, X. Wang, J. Ni, U. H. Prova, C. Wang, *et al.*, Harnessing versatile dynamic carbon precursors for multi-color emissive carbon dots, *J. Mater. Chem. C*, 2022, **10**(6), 1932–1967, DOI: 10.1039/D1TC05392B.

31 X. Hu, Y. Zhang, H. Li, J. Cao, J. Pan, C. Li, *et al.*, pH response mechanism of bifunctional fluorescent carbon quantum dots and application in cancer detection and bioself-targeting imaging, *J. Mol. Struct.*, 2024, **1308**, 137939, DOI: 10.1016/j.molstruc.2024.137939.

32 D. Zhao, X. Li, M. Xu, Y. Jiao, H. Liu, X. Xiao, *et al.*, Preparations of antibacterial yellow-green-fluorescent carbon dots and carbon dots-lysozyme complex and their applications in bacterial imaging and bacteria/biofilm inhibition/clearance, *Int. J. Biol. Macromol.*, 2023, **231**, 123303, DOI: 10.1016/j.ijbiomac.2023.123303.

33 M. Moniruzzaman and J. Kim, Synthesis and post-synthesis strategies for polychromatic carbon dots toward unique and tunable multicolor photoluminescence and associated emission mechanism, *Nanoscale*, 2023, **15**(34), 13858–13885, DOI: 10.1039/D3NR02367B.

34 H. Guo, S. Wang, L. Duan, Y. Sun and S. Chen, Synthesis of nitrogen-doped carbon quantum dot (N-CQDs) for cyanide detection, *ChemistrySelect*, 2023, **8**(37), e202302830, DOI: 10.1002/slct.202302830.

35 Y. Dong, H. Pang, H. B. Yang, C. Guo, J. Shao, Y. Chi, *et al.*, Carbon-based dots co-doped with nitrogen and sulfur for high quantum yield and excitation-independent emission, *Angew. Chem., Int. Ed.*, 2013, **52**(30), 7800–7804, DOI: 10.1002/anie.201301114.

36 Q. Xu, Y. Liu, C. Gao, J. Wei, H. Zhou, Y. Chen, *et al.*, Synthesis, mechanistic investigation, and application of photoluminescent sulfur and nitrogen co-doped carbon dots, *J. Mater. Chem. C*, 2015, **3**(38), 9885–9893, DOI: 10.1039/C5TC01912E.

37 S. Falke and C. Betzel, Dynamic light scattering (DLS): Principles, perspectives, applications to biological samples, in *Radiation in Bioanalysis*, ed. Pereira A. S., Tavares P. and Limão-Vieira P., Springer International Publishing, Cham, 2019, pp. 173–193, (Bioanalysis), DOI: 10.1007/978-3-030-28247-9_6.

38 N. Javed and D. M. O'Carroll, Long-term effects of impurities on the particle size and optical emission of carbon dots, *Nanoscale Adv.*, 2021, **3**(1), 182–189, DOI: 10.1039/D0NA00479K.

39 M. Bayati, J. Dai, A. Zambrana, C. Rees and M. Fidalgo de Cortalezzi, Effect of water chemistry on the aggregation and photoluminescence behavior of carbon dots, *J. Environ. Sci.*, 2018, **65**, 223–235, DOI: 10.1016/j.jes.2017.03.009.

40 A. Dager, T. Uchida, T. Maekawa and M. Tachibana, Synthesis and characterization of mono-disperse carbon quantum dots from fennel seeds: Photoluminescence analysis using Machine Learning, *Sci. Rep.*, 2019, **9**(1), 14004, DOI: 10.1038/s41598-019-50397-5.

41 A. R. Nallayagari, E. Sgreccia, R. Pizzoferrato, M. Cabibbo, S. Kaciulis, E. Bolli, *et al.*, Tuneable properties of carbon quantum dots by different synthetic methods, *J. Nanostruct. Chem.*, 2022, **12**(4), 565–580, DOI: 10.1007/s40097-021-00431-8.

42 J. Jiang, Y. He, S. Li and H. Cui, Amino acids as the source for producing carbon nanodots: microwave assisted one-step synthesis, intrinsic photoluminescence property and intense chemiluminescence enhancement, *Chem. Commun.*, 2012, **48**(77), 9634–9636, DOI: 10.1039/C2CC34612E.

43 A. Kurdekar, L. A. A. Chunduri, E. P. Bulagonda, M. K. Haleyurgirisetty, V. Kamisetti and I. K. Hewlett, Comparative performance evaluation of carbon dot-based paper immunoassay on Whatman filter paper and nitrocellulose paper in the detection of HIV infection, *Microfluid. Nanofluid.*, 2016, **20**(7), 99, DOI: 10.1007/s10404-016-1763-9.

44 D. R. Da Silva Souza, L. D. Caminhas, J. P. De Mesquita and F. V. Pereira, Luminescent carbon dots obtained from cellulose, *Mater. Chem. Phys.*, 2018, **203**, 148–155, DOI: 10.1016/j.matchemphys.2017.10.001.

45 H. Huang, Y. C. Lu, A. J. Wang, J. H. Liu, J. R. Chen and J. J. Feng, A facile, green, and solvent-free route to nitrogen–sulfur-codoped fluorescent carbon nanoparticles for cellular imaging, *RSC Adv.*, 2014, **4**(23), 11872–11875, DOI: 10.1039/C4RA00012A.

46 X. Sun, J. He, Y. Meng, L. Zhang, S. Zhang, X. Ma, *et al.*, Microwave-assisted ultrafast and facile synthesis of fluorescent carbon nanoparticles from a single precursor: preparation, characterization and their application for the highly selective detection of explosive picric acid, *J. Mater. Chem. A*, 2016, **4**(11), 4161–4171, DOI: 10.1039/C5TA10027E.

47 Y. Wang, S. H. Kim and L. Feng, Highly luminescent N, S- Co-doped carbon dots and their direct use as mercury(II) sensor, *Anal. Chim. Acta*, 2015, **890**, 134–142, DOI: 10.1016/j.aca.2015.07.051.

48 S. Sarkar, M. Sudolská, M. Dubecký, C. J. Reckmeier, A. L. Rogach, R. Zbořil, *et al.*, Graphitic nitrogen doping in carbon dots causes red-shifted absorption, *J. Phys. Chem. C*, 2016, **120**(2), 1303–1308, DOI: 10.1021/acs.jpcc.5b10186.

49 S. Tougaard, Practical guide to the use of backgrounds in quantitative XPS, *J. Vac. Sci. Technol., A*, 2021, **39**(1), 011201, DOI: 10.1116/6.0000661.

50 R. Fu, N. Yoshizawa, M. S. Dresselhaus, G. Dresselhaus, J. H. Satcher and T. F. Baumann, XPS study of copper-doped carbon aerogels, *Langmuir*, 2002, **18**(26), 10100–10104, DOI: 10.1021/la020556v.

51 A. G. Shard, Detection limits in XPS for more than 6000 binary systems using Al and Mg kα X-rays, *Surf. Interface Anal.*, 2014, **46**(3), 175–185, DOI: 10.1002/sia.5406.

52 Y. Yang, C. Wang, Q. Shu, N. Xu, S. Qi, S. Zhuo, *et al.*, Facile one-step fabrication of Cu-doped carbon dots as a dual-selective biosensor for detection of pyrophosphate ions and measurement of pH, *Spectrochim. Acta, Part A*, 2022, **268**, 120681, DOI: 10.1016/j.saa.2021.120681.

53 Y. Ma, Y. Cen, M. Sohail, G. Xu, F. Wei, M. Shi, *et al.*, A ratiometric fluorescence universal platform based on N, Cu codoped carbon dots to detect metabolites participating in H_2O_2-generation reactions, *ACS Appl. Mater. Interfaces*, 2017, **9**(38), 33011–33019, DOI: 10.1021/acsami.7b10548.

54 M. Azami, J. Wei, M. Valizadehderakhshan, A. Jayapalan, O. O. Ayodele and K. Nowlin, Effect of doping heteroatoms on the optical behaviors and radical scavenging properties of carbon nanodots, *J. Phys. Chem. C*, 2023, **127**(15), 7360–7370, DOI: 10.1021/acs.jpcc.3c00953.

55 W. Wu, L. Zhan, W. Fan, J. Song, X. Li, Z. Li, *et al.*, Cu–N dopants boost electron transfer and photooxidation reactions of carbon dots, *Angew. Chem., Int. Ed.*, 2015, **54**(22), 6540–6544, DOI: 10.1002/anie.201501912.

56 C. Makris, J. K. Leckrone and A. Butler, Tistrellabactins a and B are photoreactive *C* -diazeniumdiolate siderophores from the marine-derived strain *Tistrella mobilis* KA081020-065, *J. Nat. Prod.*, 2023, **86**(7), 1770–1778, DOI: 10.1021/acs.jnatprod.3c00230.